Journal of Hazardous Materials 499 (2025) 140027

Contents lists available at ScienceDirect

Journal of Hazardous Materials

journal homepage: www.elsevier.com/locate/jhazmat

Activation of lands cycle-mediated inflammation in living macrophages exposed to label-free particulate matter

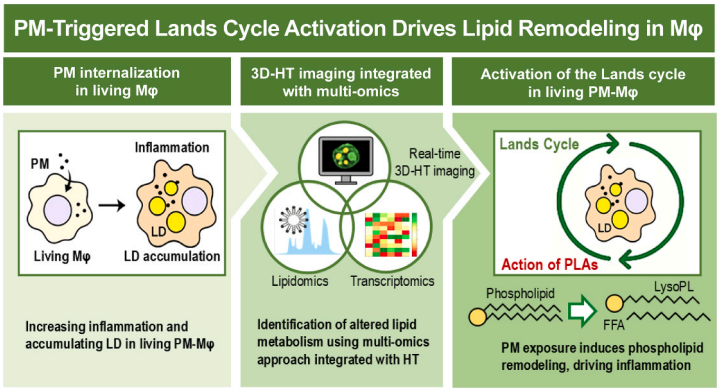
Jeongwon Park [a,c,1], Jueun Lee [b,1], Hyun-Jin Kim [c,d,1], Su-Hyun Chae [b,e], JinO Shin [a,c], Jae-Hyuk Lee [a,f], Yeongmi Cheon [a,g], Youngae Jung [b], Seul-Ki Mun [h], Jong-Jin Kim [h], Sung-Hak Kim [c,*], Geum-Sook Hwang [b,i,**], Seongsoo Lee [a,j,k,***]

[a] Aging Research Group, Honam Regional Center, Korea Basic Science Institute, Gwangju 61751, South Korea
[b] Integrated Metabolomics Research Group, Metropolitan Seoul Center, Korea Basic Science Institute, Seoul 03760, South Korea
[c] Department of Animal Science, Chonnam National University, Gwangju 61186, South Korea
[d] Center for Aging Research, Department of Dermatology, Chobanian & Avedisian School of Medicine, Boston University, MA 02118, USA
[e] Department of Chemistry, Sungkyunkwan University, Suwon, Gyeonggi 16419, South Korea
[f] Department of Pathology, School of Medicine, Stanford University, CA 94305, USA
[g] Department of Microbiology and Molecular Biology, Chungnam National University, Daejeon 34134, South Korea
[h] Department of Biomedical Science, Sunchon National University, Suncheon, Jeonnam 57922, South Korea
[i] College of Pharmacy, Chung-Ang University, Seoul 06974, South Korea
[j] Department of Systems Biotechnology, Chung-Ang University, Anseong, Gyeonggi 17546, South Korea
[k] Department of Life Science, Hanyang University, Seoul 04763, South Korea

HIGHLIGHTS

- Advanced imaging analysis: 3D-HT allows real-time visualization of altered lipid metabolism in live macrophages.
- Multi-omics integration: Lipidomics–transcriptomics integration reveals key pathways in PM-induced inflammation.
- Lands cycle activation: PM exposure induces phospholipid remodeling, driving inflammation.
- PM exposure triggers early inflammatory activation in macrophages, followed by LD accumulation.

GRAPHICAL ABSTRACT



ARTICLE INFO

Keywords:
Particulate matter

ABSTRACT

Particulate matter (PM) is a pollutant of great concern and has severe impacts on human health. Macrophages (Mφ) play a crucial role in the response to PM exposure, as they undergo metabolic reprogramming associated

* Corresponding author.
** Corresponding author at: Integrated Metabolomics Research Group, Metropolitan Seoul Center, Korea Basic Science Institute, Seoul 03760, South Korea.
*** Corresponding author at: Aging Research Group, Honam Regional Center, Korea Basic Science Institute, Gwangju 61751, South Korea.
E-mail addresses: sunghakkim@chonnam.ac.kr (S.-H. Kim), gshwang@kbsi.re.kr (G.-S. Hwang), soolee@kbsi.re.kr (S. Lee).
[1] Authors contributed equally.

https://doi.org/10.1016/j.jhazmat.2025.140027
Received 20 March 2025; Received in revised form 19 September 2025; Accepted 30 September 2025
Available online 1 October 2025
0304-3894/© 2025 The Authors. Published by Elsevier B.V. This is an open access article under the CC BY-NC license (http://creativecommons.org/licenses/by-nc/4.0/).

Macrophage
Lands cycle
3D-holotomography
Multi-omics analysis

with inflammation. However, upon exposure to PM, the metabolic changes that occur in living Mφ remain unclear. Here, we present evidence that PM activates Lands cycle-mediated inflammatory mechanisms using 3D-holotomography (3D-HT) technique integrated with multi-omics analysis. We show that internalization of PM results in abnormal lipid droplet (LD) dynamics, potentially leading to changes in lipid metabolite levels. Additionally, our multi-omics data reveal that alterations in lipid metabolism mediated by the Lands cycle leads to the increased production of inflammatory lipid mediators, including lysophospholipids, ceramides and sphingomyelins. Furthermore, by performing lipid metabolic imaging in living Mφ, we elucidated changes in the activity of altered lipid metabolism and the spatiotemporal correlation between inflammation and LD dynamics. Our findings suggest that the developed approach can provide a new experimental strategy to identify lipid metabolism biomarkers in living cells upon PM exposure.

1. Introduction

Particulate matter (PM) has a variety of adverse health effects, including metabolic disorders, such as cardiovascular diseases and diabetes [1]. Once PM has penetrated the body, it is phagocytosed by macrophages (Mφ), which are major components of the innate immune system [2]. Phagocytosis of PM leads to aberrant activity of Mφ and induces chronic stress in subcellular organelles such as lipid droplets (LD), which play a critical role as hubs for cellular metabolism [3,4]. LDs in Mφ also exhibit vigorous movement due to abnormal uptake of hazardous biological materials including oxidized low-density lipoprotein (LDL), bacteria or viruses [5,6]. However, conventional imaging methods via cell fixation can provide only limited insights into LD dynamics in living Mφ.

As a label-free imaging, 3D-holotomography (3D-HT) has become an emerging tool in live imaging fields to analyze LD dynamics [7]. A previous study proposed that this tool is also useful for the quantitative analysis of LD in living Mφ or foam cells in atherosclerosis [8]. Recent studies utilizing 3D-HT have also provided real-time tracking of intracellular PM in living Mφ [9]. However, the mechanisms underlying the correlation between PM uptake and LD dynamics remain unclear. To elucidate further LD dynamics in living PM-exposed macrophages (PM-Mφ), it is required for developing an approach based on 3D-HT technique integrated with lipidomics which provide directly visualizing and identifying lipid biomarkers.

Mφ are essential for protecting immunity and defending against immune-mediated pathological damage or exogenous stimuli like PM [10]. Mφ can produce lipid mediators such as prostaglandin E2 (PGE2), which play major roles in signal transduction and inflammatory response. Moreover, it is well known that inflammatory lipid mediators are controlled from LD during M1 polarization in Mφ [11]. Upon exposure to PM, Mφ exhibited abnormal lipid accumulation, including triacylglycerol (TAG), cholesterol and LDL thereby highlighting the pivotal role of the inflammatory response in lipid metabolism; however, the specific changes in lipid metabolism that occur during this response are unknown [12]. It is crucial to understand how altered intracellular lipid metabolites contribute to inflammatory responses triggered by PM, as well as the specific underlying mechanisms. A multi-omics approach could help to elucidate the mechanism underlying the aberrant intracellular LD dynamics associated with inflammation. Recently, combinatorial a multi-omics approach based on lipidomics or metabolomics together with transcriptomics are known as valuable tools to gain a deeper understanding of mechanistic details associated with inflammation caused by PM [13,14]. Although these studies also revealed lipidomic disruptions, including changes in the levels of phospholipids (PL), lysophospholipids (LysoPL), fatty acids, and bile acids, they primarily focused on cytotoxicity and oxidative stress, but not illustrating how PM-induced lipid metabolic changes lead to inflammation and LD accumulation. Additionally, for living PM-Mφ, a 3D-HT imaging approach integrated with multi-omics analysis to visualize and identify lipid biomarkers has not yet been attempt.

Here, we evaluated PM internalization into living Mφ over time on the basis of physical parameters, which were used to calculate a refractive index (RI) value, and quantitatively analyzed LD dynamics using 3D-HT combined with fluorescence (FL) imaging. We also revealed that altered lipid metabolism is correlated with inflammation in PM-Mφ via a multi-omics approach based on lipidomics together with transcriptomics. Furthermore, by performing quantitative time-point imaging, we determined whether inflammation in living PM-Mφ leads to enhance LD dynamics. These findings suggest an approach to quantify the changes of lipid metabolism in living cells and provide a strategy for understanding altered lipid metabolism and its effects on cellular dynamics against environmentally hazardous substances.

2. Results

2.1. PM internalization causes morphological changes in living Mφ

To visualize and track PM in living cells (Fig. 1a), we utilized the standard PM reference material, ERM-CZ100 (CZ100 as PM), which is widely used in several studies stimulating biological responses in Mφ and other cell types [15,16]. The detailed physicochemical properties of CZ100—including size distribution, metal and organic compound composition, zeta potential, and endotoxin level (Supplementary Table. 1)—support its use as a standardized label-free PM model in HT imaging [17]. Unlike EM, 3D-HT allowed us to probe the internal heterogeneity of PM particles in their native aqueous state, as evidenced by the heterogeneous RI distribution observed in segmented 3D-HT images of CZ100 (Fig. 1b). Notably, components with an RI value above 1.37, which can be tracked within cells, presented a high distribution of dry mass and volume (Fig. 1c), suggesting that label-free PM can be visualized, enabling the tracking of cellular internalization and accumulation. To compare cellular sensitivity to PM, we exposed multiple cell lines—including lung-derived (A549, H1975, SW1573), brain-derived (BV2, Neuro2A, GL-261), and RAW 264.7 macrophages—to CZ100, after exposure to 50 μg/mL of CZ100 for 24 h (Supplementary Fig. 1a). PM uptake was assessed by quantifying high-RI intracellular particles (HRIPs, RI $>$ 1.37) considered as internalized PM. Despite the presence of endogenous high-RI organelles such as LDs, RAW 264.7 cells showed the highest HRIP accumulation after exposure (Supplementary Fig. 1b). Given their pronounced PM uptake and morphological response, RAW 264.7 cells (Mφ) were chosen as the model for further analysis.

To investigate the morphological changes in the cells, their nuclei, and HRIPs among living PM-exposed Mφ (PM-Mφ), we performed both 3D visualization and quantitative analysis to evaluate physicochemical parameters, including volume, dry mass, surface area and mean RI. For this analysis, Mφ were treated with CZ100 as PM at a concentration of 50 μg/mL for 24 h. We observed a shift towards an irregular cell shape (Fig. 1d, e), a significant increase in cell volume (Fig. 1f), and a decrease in the RI of the cell (Fig. 1g) in the PM-Mφ compared with the Mφ. This reduction in cellular RI was associated with increased cell volume, a pattern also observed in our previous study [8]. In addition, we found that the total volume and mean RI of HRIPs were significantly increased in PM-Mφ, suggesting that these particles correspond to intracellular PM (Fig. 1h, i). Finally, the observed alterations in nuclear volume, surface area, mean RI, and dry mass suggested not only morphological changes but also possible changes in cellular function (Supplementary Fig. 1c-f). Together, we visualized PM internalization, along with morphological

changes and HRIP accumulation in living PM-Mφ using label-free 3D-HT imaging. Subsequently, we monitored PM internalization by this Mφ cell line over 120 min (Fig. 1j and Supplementary Video 1). The results confirmed that PM present in the medium attached to the cell membrane and was then taken up by the cells. Collectively, our findings demonstrate that PM uptake in Mφ can be visualized and quantified in real time using label-free 3D-HT imaging. This approach enables non-invasive tracking of individual particles based on RI heterogeneity, along with simultaneous analysis of internalization and cellular morphological changes. These capabilities provide a foundation for further investigation of PM-induced immune responses and subcellular remodeling.

Supplementary material related to this article can be found online at doi:10.1016/j.jhazmat.2025.140027.

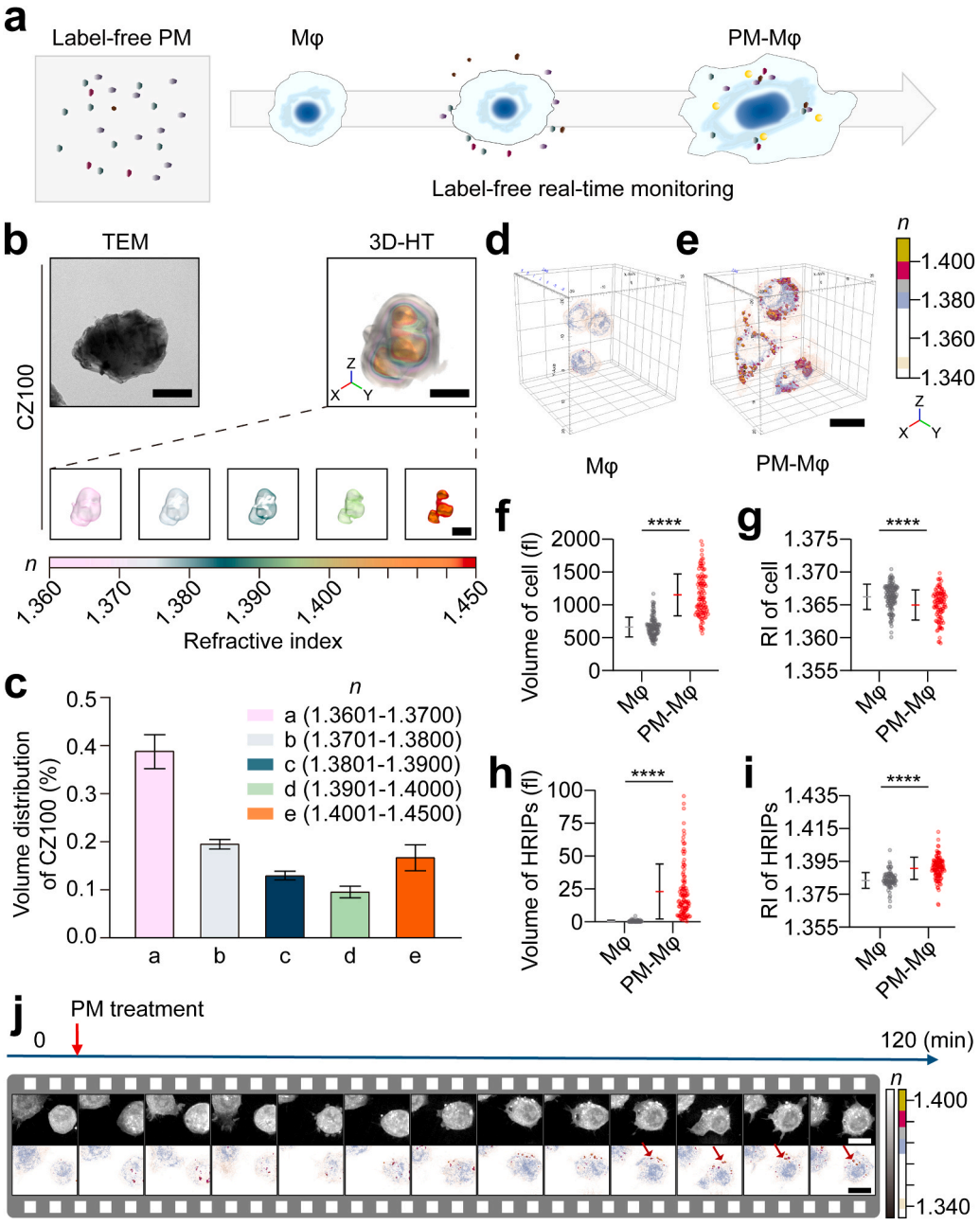


Fig. 1. Real-time monitoring of morphological changes in living Mφ after exposure to label-free PM. (a) Schematic illustration of the HT imaging workflow showing 3D RI-based visualization of label-free PM, living Mφ and PM-Mφ. Real-time monitoring was performed to track living cells over 24 h using low-coherence HT system, enabling single-cell profiling based on RI as an optical contrast. (b) Representative electron microscopy (EM) or 3D-HT images of CZ100. 3D-HT images were using RI-based masks and visualized across distinct RI ranges (1.360–1.450). Scale bars = 1 μm. (c) Quantitative volume distribution of CZ100 particles across RI ranges (1.360–1.370, 1.370–1.380, 1.380–1.390, 1.390–1.400, and 1.400–1.450). (d-e) Representative 3D-HT images of (d) untreated Mφ and (e) PM-Mφ after 24 h exposure to CZ100 (50 μg/mL). The color bar indicates particular colors depending on RI values. Scale bars = 10 μm. (f-g) Quantitative analysis of physicochemical parameters of label-free Mφ (n = 120) and PM-Mφ (n = 104). (f) Volume and (g) mean RI of the cells. (h-i) Quantitative analysis of the physicochemical parameters measured of HRIPs within the cells. (h) Volume and (i) mean RI of HRIPs. (j) Time-lapse images of 2D- (top) and 3D-HT (bottom) showing PM internalization by Mφ at 10-min interval over 2 h following treatment with CZ100 as PM (50 μg/mL). Arrows indicate PM internalization. Scale bars = 10 μm. Statistical comparisons were performed using unpaired, two-tailed t tests. *p < 0.05, **p < 0.01, ***p < 0.001, ****p < 0.0001, ns, not significant. Data are presented as mean ± SD. See also Supplementary Video 1.

2.2. PM internalization causes Mφ activation following LD accumulation

LDs play roles in a variety of cellular stress response mechanisms, including inflammation, and the lysosomes respond to external and internal stimuli to facilitate metabolic homeostasis and cellular adaptation [11,18]. To investigate whether the alterations observed in living PM-Mφ impacted subcellular organelles, we examined LD, lysosome, and autophagy, which are known to be activated upon PM internalization, and observed an increase in the numbers of puncta for Plin2, Lamp1, and Lc3b (Supplementary Fig. 2a). Notably, we also found that the accumulated LDs stained with BODIPY™ 493/503 (BODIPY) were distributed in the same region of HRIPs. (Fig. 2a, b) [7,8]. Additionally, we confirmed that the levels of intracellular lipid components, such as cholesterol and TAG, were elevated in a PM concentration-dependent manner, suggesting that the accumulated lipids may be stored in LDs and utilized through an altered cellular metabolic network (Fig. 2c and Supplementary Fig. 2b). Next, we verified the elevated expression of Plin2 and Plin5, which indicates LD accumulation, and Lamp1, which

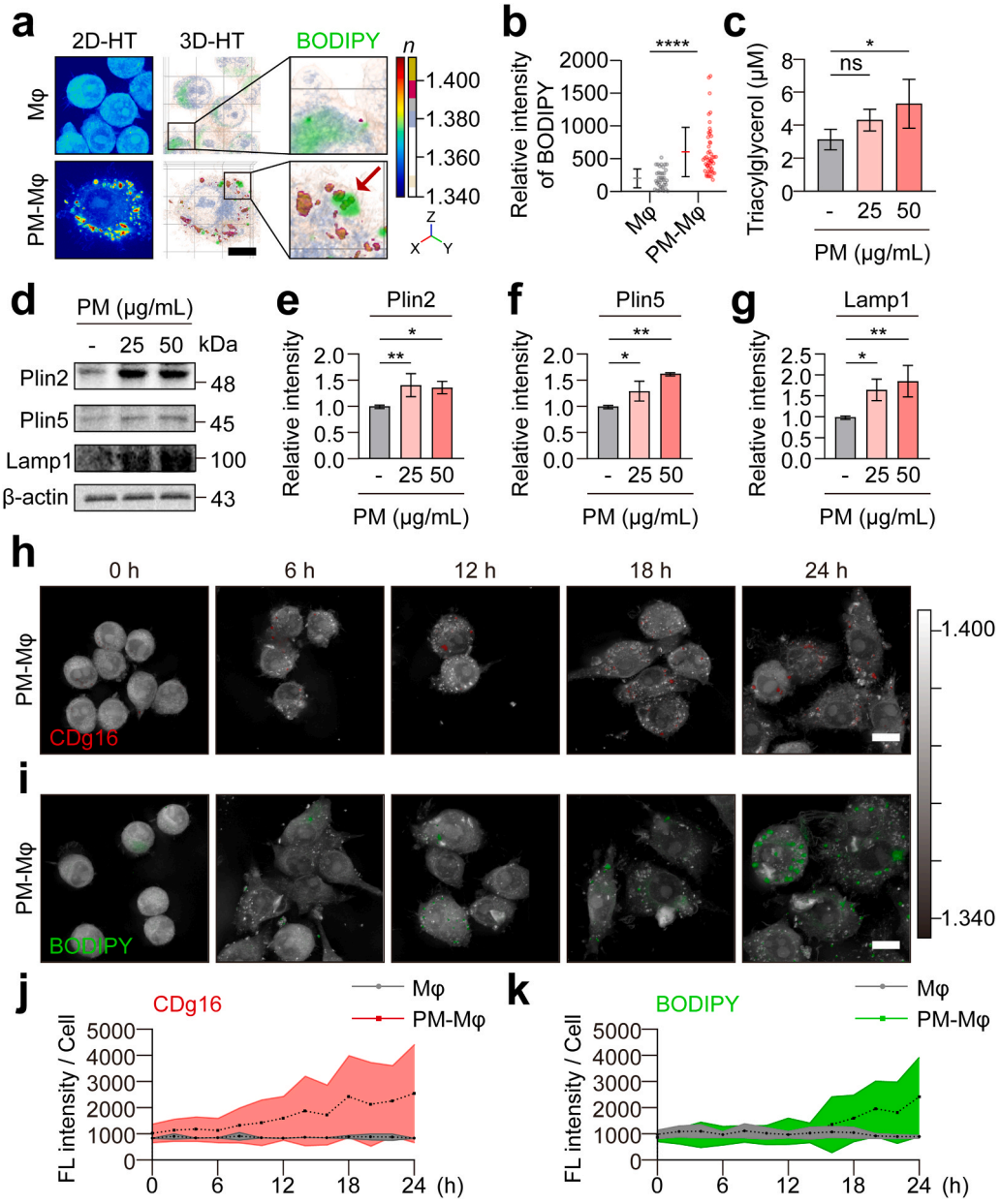


Fig. 2. Time-resolved monitoring of LD accumulation following inflammatory responses in living PM-Mφ. (a) Representative 2D- (left) and FL-combined 3D-HT (HT-FL) images (middle) of living Mφ or PM-Mφ after 24 h treatment with PM (50 μg/mL). Cells were stained with BODIPY™ 493/503 (BODIPY) in green to visualize LD. Enlarged images (right) show partial colocalization of LDs and HRIPs (arrowhead). Scale bars = 10 μm. (b) Quantitative analysis of the relative intensity of BODIPY in Mφ (n = 39) and PM-Mφ (n = 49). (c) Quantitative analysis of TAG in Mφ after treatment with 0, 25, 50 μg/mL of PM for 24 h. (d) Western blot analysis of Plin2, Plin5 and Lamp1 levels in Mφ following treatment with 0, 25 or 50 μg/mL PM for 24 h. β-actin was used as a loading control. (e-g) Quantitative analysis of protein expression levels (e, Plin2; f, Plin5; g, Lamp1), related to Fig. 2d. (h-i) Representative time point HT-FL images acquired from independent samples at each time point (0, 6, 12, 18, 24 h) following PM treatment (50 μg/mL). (h) CDg16 (red) indicates Mφ activation; (i) BODIPY marks LD accumulation. Scale bars = 10 μm. (j-k) Quantitative analysis of the relative intensity of (j) CDg16 or (k) BODIPY from independent samples in Mφ and PM-Mφ at 2-hour intervals up to 24 h. Cells were treated with PM (50 μg/mL) for up to each time point. Each time point represents a distinct sample (n > 40 per group per time point). Statistical comparisons between Mφ and PM-Mφ at each time point were conducted using unpaired, two-tailed t-tests. *p < 0.05, **p < 0.01, ***p < 0.001, ****p < 0.0001; ns, not significant. Data are presented as mean ± SD.

indicates lysosomal activation (Fig. 2d-g). These findings indicate that in response to PM exposure, living Mφ undergo significant changes in subcellular organelles and changes in biochemical properties.

PM is known to stimulate Mφ activation and enhance lipid accumulation [19]. However, little is known about the priority of inflammatory activation and LD formation in this process. To visualize inflammation response in PM-Mφ, we applied CDg16 [20] as an inflammation marker and identified increased FL signal in PM-Mφ (Supplementary Fig. 2c, d). Following this, to analyze the temporal dynamics of Mφ activation and LD formation after PM exposure, we compared relative levels of Mφ activation in red or LD in green, respectively, at multiple time points—every 2 h up to 24 h—using independent samples at each time point (Fig. 2h, i). Subsequently, we found that Mφ activation was predominant immediately after PM uptake, with progressively increasing relative levels of inflammation within the first few hours but no LD (Fig. 2j, k). This early activation was subsequently followed by an increase in LD formation, as indicated by rising relative levels of LD over time. This temporal measurement of cellular activation, and LD formation highlights a sequential relationship between inflammation and lipid metabolism in living PM-Mφ. Taken together, the time-point quantitative results and 3D-HT images indicate that PM exposure led to the aberrant dynamics of LD and the polarization of living Mφ.

2.3. Impaired lipid metabolism in PM-Mφ associated with inflammation

Given that PM exposure leads to abnormal lipid accumulation and inflammatory responses [12], we next carried out comprehensive lipidomic profiling to elucidate the lipid metabolism alterations in PM-Mφ. First, principal component analysis (PCA) score plots showed strong separation between Mφ and PM-Mφ highlighting notable differences in the lipidomic profiles (Fig. 3a). In addition, the analytical reliability of the lipidomic data was confirmed, according to tightly clustered quality control (QC) samples in both positive and negative ion modes (Supplementary Fig. 3a). A total of 234 lipids were identified in both positive and negative ion modes including phosphatidylcholines (PCs) and phosphatidylethanolamines (PEs). Of these, we observed a remarkable increase in levels of ceramides (Cers), lysophosphatidylethanolamines (LysoPEs) and lysophosphatidylcholines (LysoPCs) in PM-Mφ compared to Mφ, whereas significantly lower levels of phosphatidylglycerols (PGs), phosphatidylinositols (PIs) and free fatty acids (FFAs) were observed in PM-Mφ than in Mφ (Fig. 3b; log2 fold change $>$ 1 or $<$ -1, $p < 0.05$). Interestingly, we found that impaired lipid metabolism was linked to Mφ inflammation after exposure to PM. For example, LysoPLs such as LysoPEs and LysoPCs were substantially accumulated, while there was a substantial decrease in PE, PE-O/PE-P, PC-O/PC-P, and PI within the PL metabolism, observed in both total abundance (Fig. 3c) and individual lipid levels (Fig. 3d). Additionally, there were alterations in eicosanoid pathway and arachidonic acid metabolism in PM-Mφ. Phospholipids can be degraded by phospholipase A2 (PLA2) to generate arachidonic acid (AA, FFA 20:4) and LysoPLs such as LysoPCs and LysoPEs (Fig. 3e). The inflammatory lipid markers, prostaglandin H2 (PGH2) and PGE2, are subsequently generated through the synthesis of AA. Indeed, we observed significantly decreased levels of arachidonate-containing PLs such as PE 18:1/20:4, PE 22:6/20:4, PE-O 22:1/20:4, PI 18:0/20:4 and PI 18:1/20:4 in PM-Mφ (Supplementary Fig. 3b), while the levels of PGE2 exhibited significant increase within PM-Mφ in comparison to Mφ (Fig. 3e), concomitant with elevated patterns of intermediate metabolites, including AA (Supplementary Fig. 3c) and PGH2 (Supplementary Fig. 3d). In terms of fatty acid metabolism, the levels of very-long chain fatty acids (VLCFAs) with 22 or more carbon atoms were significantly increased in PM-Mφ compared to Mφ (Fig. 3d). Cer, SM and GlcCer in sphingolipid metabolism were significantly increased in PM-Mφ compared to Mφ (Fig. 3d). Altogether, PM exposure markedly disrupts lipid homeostasis in Mφ, characterized by accumulation of pro-inflammatory lipids (LysoPLs, AA, PGH2, PGE2) and depletion of arachidonate-containing PLs. Concomitant increases in VLCFAs and sphingolipids further indicate membrane lipid remodeling that reinforces a chronic pro-inflammatory state.

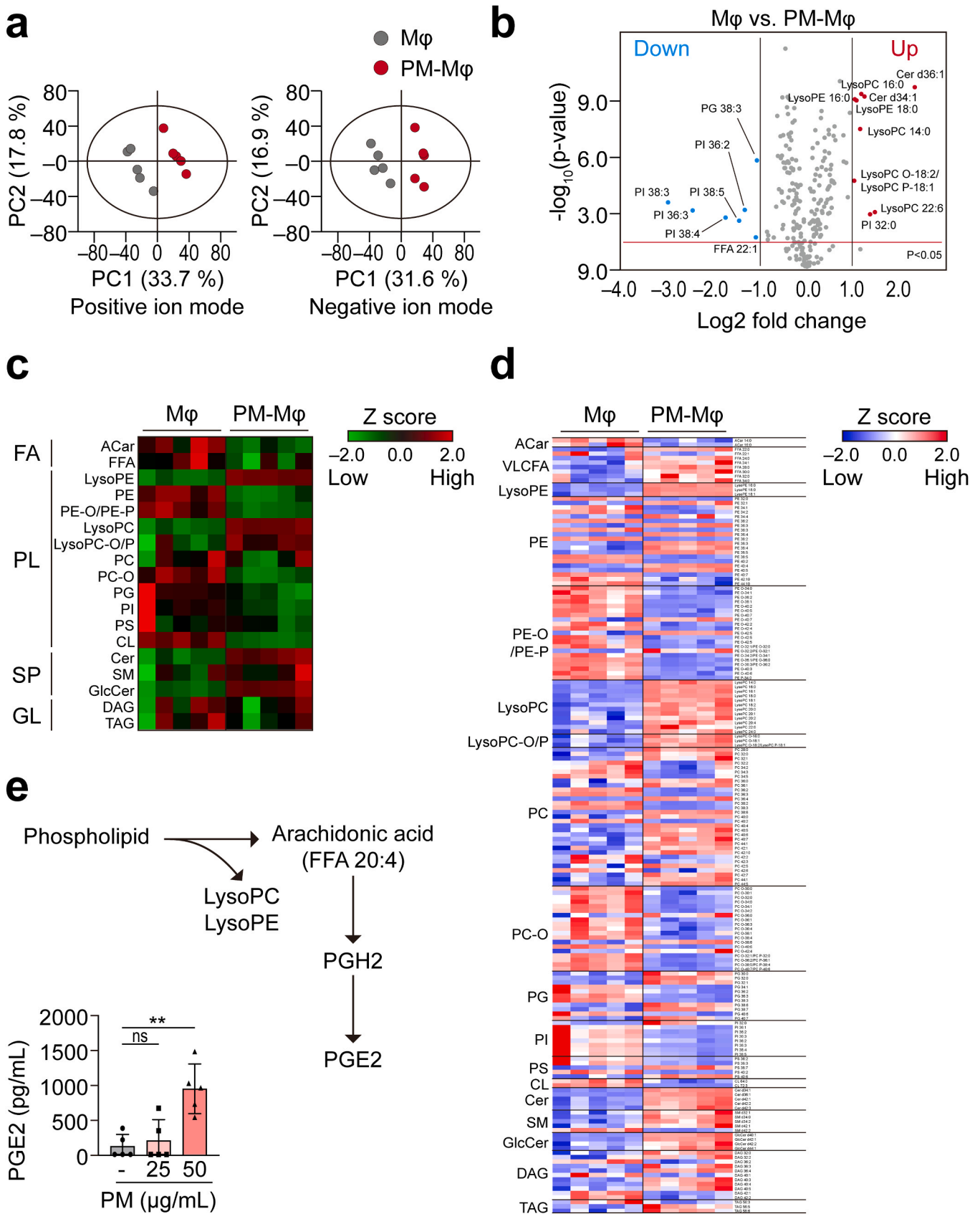
2.4. Altered gene transcription related to Lands cycle in PM-Mφ

To improve our understanding of the molecular basis of the impaired lipid metabolism and inflammation observed in PM-Mφ, we performed transcriptome analysis using RNA-seq to compare gene expression profiles (Fig. 4a). In PM-Mφ, the identified GO terms were predominantly associated with inflammation-related gene signatures (Fig. 4b and Supplementary Fig. 4a, b). Consistently, real-time PCR analysis revealed increased expression levels of genes related to inflammation, such as *Tnf*, *Ccl2*, *Ccl5*, and *Il-1α* (Supplementary Fig. 4c-f). Additionally, we identified several pathways related to inflammatory and immune responses, such as TNF, MAPK, IL-17, and NF-kappa B signaling, in the KEGG analysis (Fig. 4c). To further investigate correlations with the lipidomic results, we performed gene set enrichment analysis (GSEA) to validate the gene signatures related to lipid-mediated inflammation. Notably, we identified the eicosanoid, arachidonic acid metabolism, and lysophospholipid pathways, which are linked to inflammation; this was consistent with the notable changes observed in our lipidomics results (Fig. 4d-f). To validate these findings in our GSEA results, we analyzed representative gene sets for each pathway. We observed significant increases in the expression of inflammatory lipid-related factors, including *Ptger2*, *Ptgir*, *Ptgs2*, *Ptges*, *Alox15*, *Pla2g4b*, *Pla2g5*, and *Pla2g2e* (Fig. 4g). These alterations are positively correlated with the eicosanoid pathway and arachidonic acid metabolism, particularly following Lands cycle activation, and may drive the production of inflammatory lipid markers in PM-Mφ. In addition, we confirmed increased expression of lysophospholipid pathway-related genes such as *Il-6*, *Hbegf*, *Bcar1*, *Src*, *Jun*, *Pik3cb*, *Mmp9*, *Gsk3B,* and *Adcy3*, which corresponded to elevated LysoPL levels lipidomic analysis (Fig. 4g). To further validate these findings, we performed qRT-PCR after treating PM-Mφ with increasing concentration of PM (0, 1, 10, 50, 100, and 200 μg/mL). The expression levels of *Ptgs2*, *Pla2g5*, and *Pla2g2e* increased in a dose-dependent manner, supporting their association with PM-induced lipid remodeling and inflammation (Supplementary Fig. 4g-i). Together, these results indicate that PM exposure upregulates Lands cycle–related phospholipases and inflammatory lipid pathways, with dose-dependent induction of *Ptgs2*, *Pla2g5*, and *Pla2g2e*, potentially sustaining lipid-driven inflammation in PM-Mφ.

2.5. Elevated PLA2 activity related to the Lands cycle in PM-Mφ

To validate the observation that the Lands cycle was activated, as indicated by our multi-omics analysis and the observed increase in the levels of *Pla2* gene family in PM-Mφ, we utilized two fluorescent PLA substrates, Red/Green BODIPY™ PC-A2 (PC-A2) and PED-A1, to monitor PLA enzyme activity (Fig. 5a and Supplementary Fig. 5a). We visualized and measured PLA activity on the basis of the FL signals released upon substrate hydrolysis by PLA enzymes. This approach allowed us to perform both quantitative analysis and intracellular localization of products, including LysoPC and FFAs, within PM-Mφ (Fig. 5b-d and Supplementary Fig. 5b, c) [21–23]. As expected, significantly stronger FL signals for LysoPC in red and FFAs in green were observed in or around PM-Mφ, suggesting that the Lands cycle is activated and that LysoPLs underwent substantial accumulation (Fig. 5b-d and Supplementary Fig. 5b, c). These results, which are consistent with the findings obtained in our multi-omics analysis, suggest that there is a link between the accumulation of LysoPLs such as LysoPEs and LysoPCs and the observed reduction in the levels of specific PLs.

Next, we performed real-time HT-FL imaging to investigate whether the amount of LysoPC and FFA digested in PM-Mφ increased and whether the intracellular localization of LysoPC and FFA changed (Fig. 5e-g and Supplementary Video 2). Over time, LysoPC and FFA



(caption on next page)

Fig. 3. Dysregulation of lipid metabolism in PM-Mφ. (a) PCA score plots discriminating Mφ (gray) and PM-Mφ (red) in positive ion mode (left: R2X, 0.515; Q2, 0.152) and negative ion mode (right: R2X, 0.484; Q2, 0.0858). (b) Volcano plot highlighting significantly decreased levels of lipids (left) and increased levels of lipids (right) in PM-Mφ group compared to Mφ group. The annotated blue and red dots are significantly changed and the threshold set to −1 and 1 for log2 fold change. (c) Heatmap representing total abundance of lipid subclass in Mφ and PM-Mφ. (d) Heatmap showing significant changes in 173 individual lipid levels between Mφ and PM-Mφ ($p < 0.05$). p-values were determined using Student's *t*-test. Data are expressed as row Z-scores, collected from five biologically independent experiments per condition. (e) Degradation pathway of phospholipids into PGE2 and changes in the concentration of PGE2 in Mφ after being untreated or treated with 25 or 50 μg/mL of PM for 24 h. Data are shown as mean ± SD. FA, fatty acyls and conjugates; PL, phospholipids; SP, sphingolipids; GL, glycerolipids; Acar, acylcarnitines; FFA, free fatty acids; LysoPE, lyso-phosphatidylethanolamines; PE, phosphatidylethanolamines; PE-O, plasmanyl-phosphatidylethanolamines; PE-P, plasmenyl-phosphatidylethanolamines; LysoPC, lyso-phosphatidylcholines; PC, phosphatidylcholines; PC-O, plasmanyl-phosphatidylcholines; PC-P, plasmenyl-phosphatidylcholines; PG, phosphatidylglycerols; PI, phosphatidylinositols; PS, phosphatidylserines; CL, cardiolipins; Cer, ceramides; SM, sphingomyelins; GlcCer, glucosylceramides; DAG, diacylglycerols; TAG, triacylglycerols. PLA2, phospholipase A2; prostaglandin H2, PGH2; prostaglandin E2, PGE2.

increased in abundance and moved into the cells, suggesting that the PLA2-mediated degradation of PLs likely generates AA, which may lead to LysoPL formation and the synthesis of inflammatory lipid markers such as PGH2 and PGE2. To directly assess the role of PLA2 activity in this process, we treated PM-Mφ with selective PLA2 inhibitors—Varespladib (5 μM) [24] and Alminoprofen (200 μM) [25]—and evaluated LD formation and PGE2 production using HT-FL imaging and biochemical assays (Supplementary Fig. 6). Interestingly, although PLA2 inhibition has mild effects to alter LD accumulation (Supplementary Fig. 6a, c), LysoPC levels were markedly reduced in the inhibitor-treated groups (Supplementary Fig. 6b, d). Consistently, PGE2 production was also suppressed following PLA2 inhibition (Supplementary Fig. 6e), supporting that PLA2 activity is functionally required for the generation of inflammatory lipid mediators, but not for LD biogenesis.

Supplementary material related to this article can be found online at doi:10.1016/j.jhazmat.2025.140027.

Additionally, lipidomic profiling revealed no significant changes in LysoPC and LysoPE levels after treatment with PLA2 inhibitors (Supplementary Fig. 7a). In contrast, both LysoPC-O and LysoPE-O were markedly reduced (Supplementary Fig. 7a). FFA profiles (Supplementary Fig. 7b) and glycerophospholipid profiles (Supplementary Fig. 7c) also showed no substantial alterations following PLA_2 inhibition. These findings indicate that PLA2 inhibition preferentially affects LysoPL-O species while leaving major lipid classes largely unchanged, thereby suppressing PM-induced inflammatory responses and supporting a mechanistic link between the Lands cycle and LysoPL-O metabolism. These findings suggest that the Lands cycle may be a pathway through which the inflammatory response is sustained via lipid mediator production in PM-Mφ.

3. Discussion

Here, we used a 3D-HT imaging approach integrated with multi-omics analysis to identify alterations in lipid metabolism and visualize lipid biomarkers in living PM-Mφ (Fig. 6). In addition, we found that the levels of PLA2-targeting PLs, including PCs and PEs are increased in living PM-Mφ. The PLA2-mediated degradation of PLs likely generates AA, which may lead to LysoPL formation and the synthesis of inflammatory lipid markers such as PGH2 and PGE2. Overall, these findings suggest that the Lands cycle may be a pathway through which the inflammatory response is activated and inflammatory lipid mediators in LDs are produced in PM-Mφs. The results of our study demonstrated that PM activates Lands cycle-mediated inflammation. We provide spatio-temporally resolved evidence that PM exposure dynamically induces LD accumulation and Lands cycle-mediated production of inflammatory mediators, reflecting system-wide remodeling of lipid metabolism and contributing to Mφ immunometabolic reprogramming. Moreover, the elevated levels of LDs, PGE2, and specific LysoPLs suggest their potential as lipid biomarkers for monitoring PM uptake and inflammation. Together, our findings establish a mechanistic and visual framework for understanding how PM disrupts lipid homeostasis and promotes inflammation in Mφ, paving the way for lipid-based diagnostic or therapeutic strategies in PM-related diseases.

Rapid advances in multi-omics technologies have been effectively utilized in recent studies investigating the adverse health effects and molecular mechanisms of complex hazardous materials [26–28]. In particular, this approach has demonstrated the existence of associations among lipid metabolic reprogramming, inflammation, and ROS in response to PM exposure in various cell models [29–33]. Through integrated lipidomic and transcriptomic analysis, we observed PLA2 activation and an increase in PGE2 synthesis due to alterations in the Lands cycle upon the uptake of PM by Mφ (Figs. 3–4). Prolonged exposure to stimuli leads to lipid metabolism reprogramming, which involves not only pre-existing enzymes but also transcriptionally-regulated events that culminate in the expression of specific protein effectors. In PM-Mφ, we observed significant upregulation of PLA2-related genes, including *Pla2g5* and *Pla2g2e* (Fig. 4g), which code for enzymes that hydrolyse PLs into LysoPLs and AA. Furthermore, FL imaging revealed a significant increase in the activity of PLA2 enzymes, such as PC-A2 and PED-A1 (Fig. 5 and Supplementary Fig. 5). At the lipid levels, PM entry into Mφ resulted in a significant increase in LysoPC and LysoPE levels, as well as increased abundance of AA, ultimately leading to a significant increase in proinflammatory PGE2 (Fig. 3 and Supplementary Fig. 3).

Since the late 1950s, when William E.M. Lands first discovered a unique metabolic pathway for PL recycling, several studies have reported the critical role of the Lands cycle in inflammation and immune responses [34]. Interestingly, PLA2s play a key role in the synthesis and degradation of LDs, thereby regulating LD homeostasis [35]. The synthesis of new PLs to stabilize the LD monolayer structure is essential for LD biosynthesis. cPLA2α promotes LD expansion by enabling PL remodeling in the ER membrane, including deacylation and reacylation reactions [36]. In particular, the accumulation of LysoPLs, including LysoPCs, LysoPEs, and LysoPAs, produced by PLA2, offers structural support for the initiation of nascent LD budding [36,37]. Indeed, activation of cPLA2α via phosphorylation leads to LD formation, whereas inactivation of cPLA2α reduces LD formation [38–41]. LysoPLs, such as LysoPCs and LysoPEs, function both as intermediates in lipid metabolism and as potent pro-inflammatory mediators implicated in a wide range of human diseases [42]. Saturated and monounsaturated LysoPC species (e.g., 16:0, 18:0, 18:1) promote leukocyte and monocyte chemotaxis [43,44], activate neutrophil NADPH oxidase, enhance ROS and cytokine production, and drive systemic inflammation [45], while LysoPEs, particularly LysoPE 18:1, has been linked to TH17 cell differentiation and autoimmune neuroinflammation [46]. In addition, LysoPLs have been implicated in the development of inflammatory diseases, cardiovascular disorders, neurodegenerative diseases, and cancer [42,47]. Dysregulated PLA2 activity can elevate LysoPCs in oxidized LDL, contributing to endothelial dysfunction and atherosclerosis [48], and human studies show that short-term PM2.5 exposure alters circulating LysoPL subclasses, mediating pro-atherosclerotic biomarkers [49]. Collectively, these findings suggest that PM-induced perturbations in the Lands cycle and LysoPL metabolism are central to inflammatory and cardiovascular responses. These findings, although derived from cell-based analyses, may have broader implications for PM-associated cardiovascular disease. In particular, the presence of CDg16—a Mφ activation marker previously identified in lipid-rich

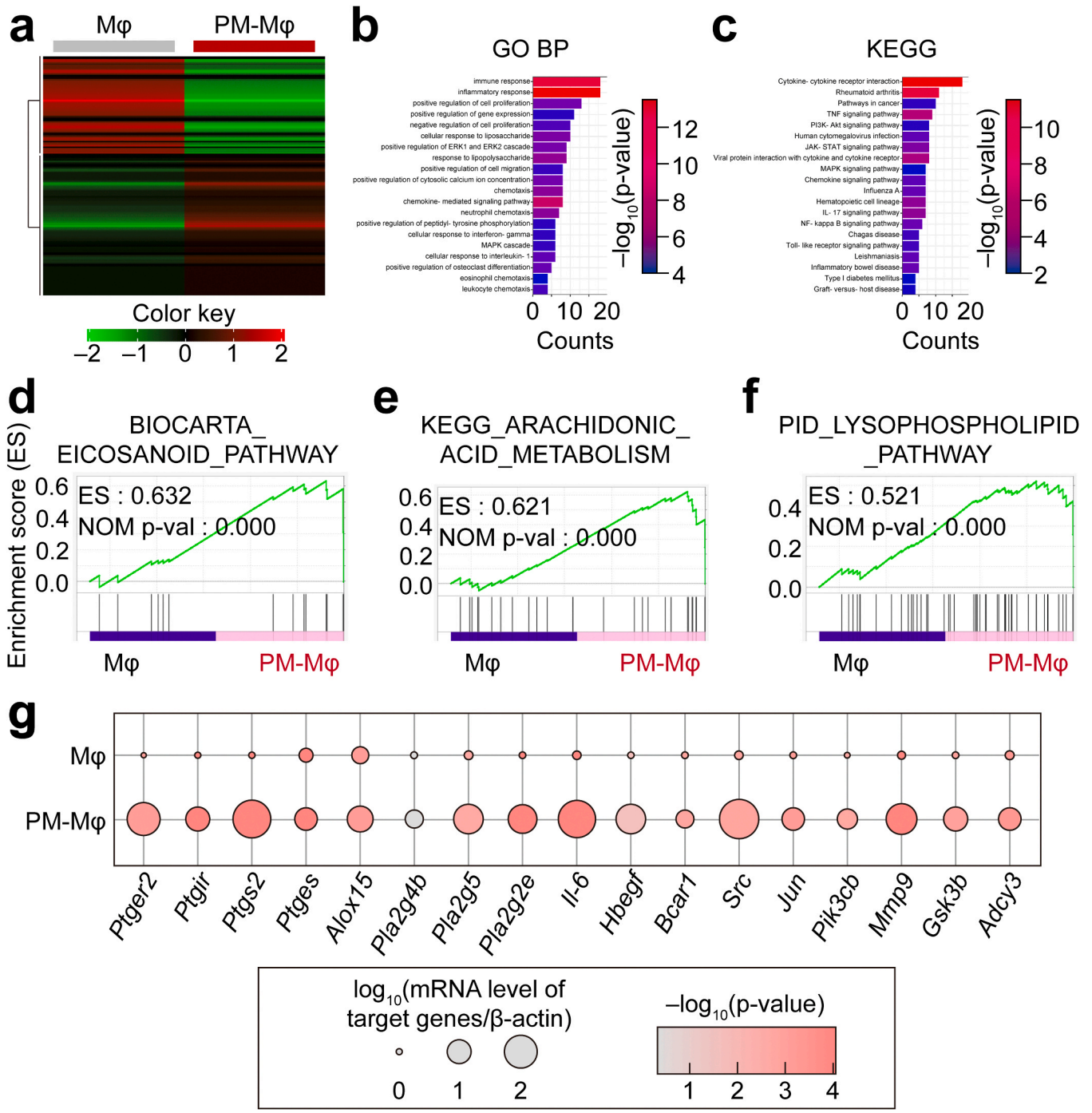


Fig. 4. Transcriptome alterations related to activation of the lands cycle in PM-Mφ. (a) Heatmap showing the differential expression levels of genes in Mφ and PM-Mφ. (b-c) Horizontal bar charts displaying the top 20 significant pathways based on the cutoff determined for the genes whose expression was significantly upregulated in PM-Mφ compared with Mφ. (b) GO-BP and (c) KEGG pathway analysis. GO-BP, Gene Ontology biological process; KEGG, Kyoto Encyclopedia of Genes and Genomes. The Y-axis shows the names of the signaling pathways or functions, and the X-axis shows the number of genes assigned to a category annotated in the network. Colors indicate p-values, with a red bar indicating a higher significance level. (d-f) Gene set enrichment analysis revealed that genes related to activation of the lands cycle were positively enriched in indicated PM-Mφ. Significantly enriched pathways included: (d) BIOCARTA EICOSANOID PATHWAY, (e) KEGG ARACHIDONIC ACID METABOLISM, and (f) PID LYSOPHOSPHOLIPID PATHWAY. ES, enrichment score; NOM p-val, nominal p-value. (g) qRT-PCR analysis of selected genes from the enriched pathways related to Fig. 4d-f. Balloon size indicates the - $\log_{10}$ relative mRNA expression level (normalized to β-actin). Colors of the plots indicate the – $\log_{10}$ p-value. Statistical comparisons were conducted using unpaired, two-tailed t-tests.

atherosclerotic plaques—together with altered lipid mediators such as LysoPCs and PGE2, suggests a potential mechanistic link between PM-induced lipid remodeling, vascular inflammation, and atherosclerosis. Given that phospholipid remodeling pathways like the Lands cycle regulate both inflammatory signaling and metabolic states, and that dysregulated PLA2 activity can elevate LysoPCs in oxidized LDL leading to endothelial dysfunction, these molecular alterations may serve as indicators of environmentally driven immune-metabolic dysfunction and as candidate biomarkers for future translational research. Furthermore, sphingolipid metabolism, indicated by Cer, SM, and GlcCer levels, was increased in PM-Mφ. This effect may have been associated with increased expression of ceramide kinase, which synthesizes ceramide

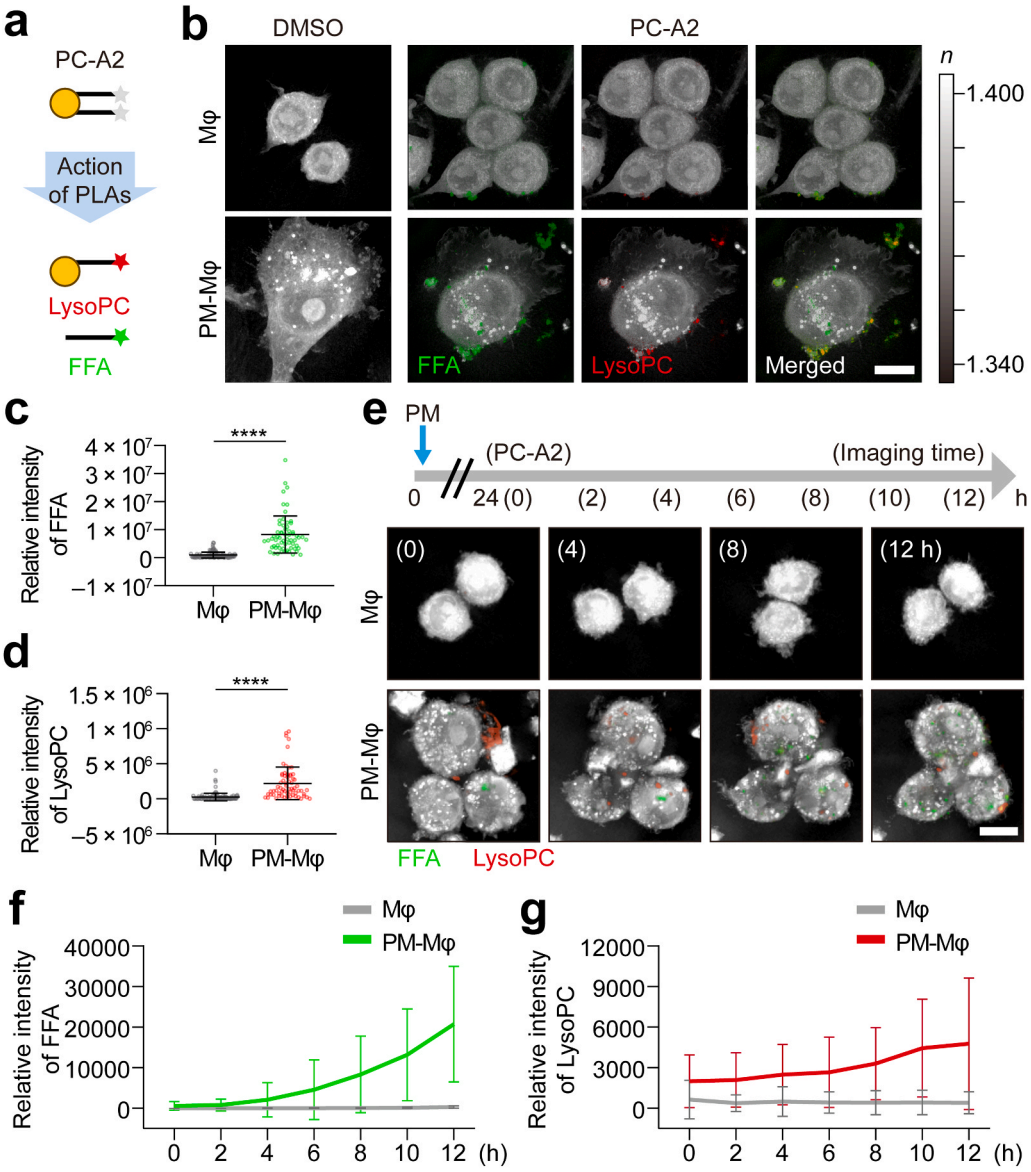


Fig. 5. Activation of the Lands cycle is accompanied by inflammatory LD dynamics in PM-Mφ. (a) Schematic of PLA activity visualization using PC-A2. PC-A2 is a dye-labeled phospholipid used to measure PLA2 activity in living cells. The cleavage products derived from PC-A2 are FFA (green) and LysoPC (red), respectively. (b) Representative HT-FL images of Mφ or PM-Mφ stained with DMSO or PC-A2 to visualize the activity of PLAs. The grayscale color maps show RI distributions of the HT images. Scale bar = 10 μm. (c-d) Quantitative analysis of the relative intensities of (c) FFA and (d) LysoPC generated from PC-A2 in Mφ (n = 111) and PM-Mφ (n = 63). (e) Representative time-lapse HT-FL images to visualize PLA activity in Mφ and PM-Mφ treated with PC-A2 for 12 h. (f-g) Quantitative analysis of the relative intensities of (f) FFA and (g) LysoPC in time-lapse imaging of Mφ (n > 25) and PM-Mφ (n > 25). Scale bar = 10 μm. Statistical comparisons were conducted using unpaired, two-tailed t-tests. *p < 0.05, **p < 0.01, ***p < 0.001, ****p < 0.0001, ns, not significant. All values are presented as mean ± SD. See also Supplementary Video 2.

1-phosphate and leads to cPLA2α phosphorylation and enhanced LD biosynthesis [41]. Additionally, Toll-like receptor 4 (TLR4) activation occurs as a part of the Mφ inflammatory response. TLR4 activation stimulates fatty acid synthesis, which subsequently promotes sphingolipid biosynthesis. Notably, elevated levels of Cer contribute to increased proinflammatory cytokine production [50].

The accumulation of VLCFAs is also associated with the inflammatory response in Mφ following PM exposure. In previous studies, treatment of Mφ with lipopolysaccharide led to an increase in saturated long-chain fatty acids and polyunsaturated fatty acids, along with the upregulation of fatty acid biosynthesis enzymes such as fatty acid synthetase (FASN), fatty acid desaturase 2 (FADS2), and elongation of very long-chain fatty acids 7 (ELOVL7) accompanied by elevated levels of saturated and monounsaturated VLCFAs [51]. Taken together, these findings suggest that exposure of Mφ to PM induces changes in lipid metabolism, including activation of the Lands cycle, at the transcriptomic and lipidomic levels. These alterations may be linked to inflammation and LD accumulation.

Mφ express multiple PLA2 isoforms that play essential roles in immune regulation, including lipid-mediated signaling for immune activation, particle uptake, microbial clearance, and membrane repair [52–54]. PLA2 activity generates arachidonic acid, a precursor of pro-inflammatory prostaglandins such as PGE2, while LysoPCs can stimulate chemokine production in endothelial cells [43] and cytokine release in Mφ [44]. Phagocytic stimuli further promote the release of eicosanoids, including arachidonic acid and PGE2 [55], which not only mediate inflammation but also directly enhance phagocytosis and antimicrobial activity in Mφ-like cells [56,57]. Collectively, these

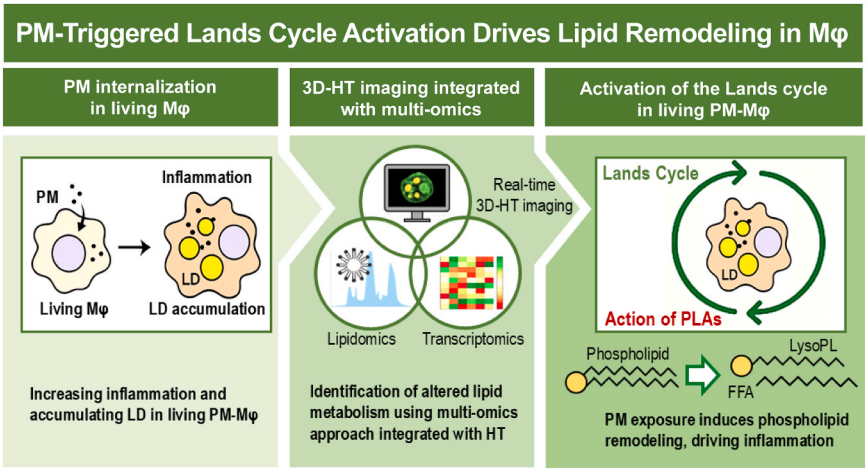


Fig. 6. Dynamic changes in lipid metabolism in PM-Mφ during inflammation. Illustration of lipid metabolism regulation in PM-Mφ with induction of inflammation and LD accumulation. Following PM internalization, Mφ activation increases the activity of phospholipid-related Lands cycle pathways, leading to increased production of lipid metabolites, which contribute to either the synthesis of inflammatory lipid mediators or LD accumulation.

findings indicate that PM exposure reprograms inflammatory signaling and lipid metabolism in Mφ, thereby augmenting cytokine production and phagocytic capacity through coordinated transcriptional and lipidomic adaptations.

Although lipid reprogramming caused by PM has recently been recognized as a crucial driver of inflammation in Mφ, the spatiotemporal changes and mechanisms involved remain unclear. By using HT, we tracked PM uptake and investigated the dynamics of inflammation and LD accumulation in living PM-Mφ. Recently, HT has emerged as a promising tool for real-time monitoring of the effects of environmentally hazardous materials. The dynamic imaging capabilities of HT provide a unique opportunity to observe cellular processes in response to hazardous materials in real-time, offering critical insights into the complex behaviors of organelles, such as LD, and immediate metabolic marker changes in living cells [9,58,59].

In this study, we analyzed PM in living PM-Mφ and determined the RI values of HRIPs. This allowed us to quantify the volume of internalized PM and changes in cellular properties (Figs. 1, 2). We also demonstrated the temporal correlation between LD dynamics and inflammation patterns, suggesting that LD accumulation following cellular activation-driven by the buildup of TAG or cholesterol in LD may generate inflammatory lipid mediators like PGE2 and regulate intracellular stresses such as ROS and lipid toxicity. We next sought to improve conventional approaches by integrating 3D-HT with multi-omics analysis to identify specific changes in lipid metabolism (Figs. 3–5), thereby demonstrating that 3D-HT is a valuable tool for identifying and discovering lipid metabolism biomarkers associated with the entry of harmful substances into living cells.

Recent studies have shown that biological hazards, such as viruses causing severe acute respiratory syndrome (SARS), Middle East respiratory syndrome (MERS), influenza, and acquired immunodeficiency syndrome (AIDS), can induce inflammation and metabolic changes in cells [60,61]. These biological hazards exploit host cell lipids and synthesis machinery to facilitate their replication and pathogenesis. Similarly, environmental hazards, including heavy metals and nanoplastics, can interfere with lipid metabolism, leading to the accumulation of toxic lipid species and subsequent inflammation [62,63]. Additionally, endocrine-disrupting chemicals can alter lipid homeostasis, resulting in metabolic dysfunction and inflammatory responses within the cell [64]. These studies underscore the importance of lipid metabolic reprogramming in response to both biological and environmental hazards. Therefore, real-time monitoring of lipid metabolic changes through the new analytical platform of 3D-HT integrated with multi-omics is essential for elucidating the cellular responses mechanisms and offering potential therapeutic targets.

Despite its potential, HT is associated with several technical challenges that must be overcome before it is applied more widely and substantially impact research on environmental pollutants, such as PM. First, it is crucial to develop faster image reconstruction algorithms and robust segmentation tools for organelles or PM and integrate with other imaging technologies. Integrating these analyses with other label-free imaging techniques, such as Raman spectroscopy and atomic force microscopy, will provide more diverse information about lipid profiles at the single-cell level [65,66]. While 3D-HT offers label-free, quantitative refractive index–based imaging, its spatial resolution and molecular specificity remain lower than those achievable with super-resolution microscopy. Consequently, optimal application of 3D-HT may involve integration with complementary high-resolution, molecule-specific modalities to achieve both quantitative and mechanistic insights. Additionally, standardization of HT data analysis for hazardous materials using RI2FL profiling [67] is necessary to pave the way for broader applications in the biomedical field. We believe that the further studies will contribute to the application of label-free imaging or real-time monitoring techniques for environmentally hazardous materials. Furthermore, real-time monitoring and quantitative analysis of dynamic organelles in living cells can be employed to evaluate the interactions of organelles with environmentally hazardous materials in real time. As the experiments were conducted in cell culture systems, future studies using in vivo animal models or human samples will be needed to better reflect the complexity of tissue- or organism-level responses. Although standardized PM was used to ensure consistency, the heterogeneous physicochemical characteristics of real-world PM—such as differences in composition, size, solubility, and concentration—should be considered to enhance environmental relevance. Notably, experimental designs should incorporate PM exposure conditions that closely simulate real-world environments, with protocols optimized for several studies using cells and model animals [68,69]. Finally, the mechanisms underlying the rapid alterations in lipid metabolism and the effects on metabolism-related organelles such as mitochondria and LD that occur after exposure to hazardous materials are unclear. This gap in knowledge can be addressed by integrating artificial intelligence-3D-HT analysis techniques and recognition algorithms [70] with spatial multi-omics in a single cell [71].

The integration of 3D-HT with multi-omics analysis is in its initial stages but shows strong potential to advance research on environmentally hazardous materials, such as PM and microplastics, in living cells. Identifying lipid metabolism biomarkers affected by these substances could enhance our understanding of metabolic diseases and improve

diagnostic and prognostic precision.

4. Experimental section

4.1. Cell cultures

For cell culture, murine macrophages (RAW264.7) were obtained from Korean Cell Line Bank (KCLB). RAW264.7 cells were cultured in high glucose, GlutaMAX™ Supplement, pyruvate (DMEM, Gibco™) containing 10 % fetal bovine serum (FBS, Gibco™) and 1 % penicillin-streptomycin (p/s, Gibco™). Human lung cancer cell lines such as A549, H1975, and SW1573 were obtained from ATCC [72,73] and cultured in RPMI containing 10 % FBS and 1 % p/s. Either the BV2 mouse microglial cell line and the Neuro2A mouse neuroblastoma cell line [74,75] were cultured in DMEM containing 10 % FBS and 1 % p/s. The GL261 mouse glioma cell line [76] was cultured in DMEM/F12 (Thermo Fisher) containing 10 % FBS and 1 % p/s.

4.2. Reagents and treatments

For PM treatment, stock solutions were prepared by suspending PM (ERM-CZ100, Sigma) in phosphate-buffered saline (PBS) at a concentration of 10 mg/mL. These stock solutions were added to the cell culture medium at final concentrations of 25 μg/mL or 50 μg/mL. The following dyes were used: BODIPY 493/503 (BODIPY, 1 μg/mL, Thermo Fisher), LysoTracker™ Red DND-99 (LysoTracker, 1 μg/mL, Thermo Fisher), CDg16 (1 μM, Senpro). The cells were stained with dyes for 30 min, washed twice with PBS and imaged. To visualize PLA activity in living cells, PC-A2 (0.5 μM, Sigma) or PED-A1 (2.5 μM, Sigma) in HBSS was used to replace the cell culture medium. For inhibition experiments, Varespladib (5 μM, MedChemExpress) and Alminoprofen (200 μM, MedChemExpress) were applied.

4.3. Immunocytochemistry and western blot analysis

For immunocytochemistry, the cells were fixed in 4 % PFA containing 4 % sucrose for 30 min and then washed in PBS. The cells were and incubated in permeabilization buffer (0.1 % Triton X-100, 0.5 mg/mL sodium deoxycholate in PBS, pH 7.4) for 15 min at room temperature. The primary antibodies used were as follows: anti-Plin2 (1:100, PROGEN), anti-Lamp1 (1:100, Abcam), and anti-Lc3b (1:100, Cell Signaling Technology). Incubation with primary antibodies was performed at 4 °C overnight. All secondary antibodies (1:1000, Molecular Probes) were incubated with the cells for approximately 1 h at room temperature. After washing with PBS, ProLong™ Diamond Antifade Mountant with DAPI (Invitrogen™) was used for nuclear staining. Confocal images were obtained with a Leica TCS SP5 AOBS confocal microscope equipped with 40 × or 100 × inverted NX oil lenses. For western blot analysis, cell lysis was performed using a combination of RIPA buffer and phosphatase inhibitor cocktail (ApexBio), and the protein concentration of the lysed cells was determined via a BCA protein assay kit (Thermo Fisher). The following primary antibodies were used: anti-Plin2 (1:1000, PROGEN), anti-Plin5 (1:1000, PROGEN), anti-Lamp1 (1:1000, Abcam), and anti- β-actin (1:5000, Santacruz). All primary antibodies were diluted in 0.5 % BSA in Tris-buffered saline with 0.1 % Tween 20 (TBST) and incubated with the membrane at 4 °C overnight. All secondary antibodies (1:5000, Jackson ImmunoResearch Laboratories) were incubated with the samples for 1 h at room temperature.

4.4. HT combined with fluorescence imaging

For HT combined with FL imaging, PM was seeded onto 50 mm imaging dishes (TomoDish, Tomocube) at 50 μg/mL. 3D-HT images were obtained using a commercial instrument (HT-2H, Tomocube), which is based on Mach–Zehnder interferometry and is equipped with a digital micromirror device (DMD) operated with commercial software (TomoStudio™, Tomocube). 3D RI distribution reconstruction of the samples was carried out via HT on the basis of the Fourier diffraction theorem, following previously established procedures [77]. To measure the physical properties of each PM particle, AI-based RI segmentation was performed using commercial software (TomoAnalysis™ version 1.3.25, Tomocube). Each PM particle was detected and analyzed on the basis of voxels, which were reconstructed from the RI values. For HT combined with FL imaging of living PM-Mφ, 3D-HT images of living cells were obtained according to previously described protocols [8]. Living cells were treated with culture medium supplemented with 50 μg/mL PM for 24 h, washed twice to avoid interference from floating PM in the dish, and then subjected to 3D-HT imaging. All 3D-HT imaging was performed using TomoStudio™ (Tomocube) as described previously [8]. For time-lapse HT imaging, living cells were seeded on a glass bottom dish (35 mm glass bottom dish with 10 mm microwell #1.5 cover glass, Cellvis). After PM treatment, living cells were imaged at 10-min intervals for 24 h using a low-coherence HT imaging system (HT-X1, Tomocube). The HT-X1 system was equipped with a motorized 40x NA 0.95 objective lens (UPLXAPO40X, Olympus), a 450-nm LED illumination module merged with DMD at the pupil plane and a custom-designed condenser lens (NA = 0.72, working distance = 30 mm). A stage-top incubator (STXG-WSKMXA22B-E, TOKAI HIT, Shizuoka) was added to the stage of HT-X1 system to maintain the temperature, humidity, and CO_2 concentration (5 %). 2D-HT images of the living cells were reconstructed with dedicated software (TomoAnalysis version 1.7.13, Tomocube).

4.5. Transcriptomics analysis

For RNA-sequencing, total RNA (1 mg) was processed for mRNA sequencing library preparation using the MGIEasy RNA Directional Library Prep Kit (MGI) following the manufacturer's instructions. The methods involved poly-A mRNA purification, fragmentation, cDNA synthesis, adapter ligation, and PCR enrichment. The resulting cDNA library was quantified, circularized, and converted to DNA nanoballs (DNBs) for sequencing on the MGIseq system with 150 bp paired-end reads. The raw reads were preprocessed using Skewer ver 0.2.2 [78] and mapped to the reference genome using STAR ver 2.5 [79]. Gene expression was quantified using Cuffquant in Cufflinks ver 2.2.1 [80], and differential expression analysis was performed using Cuffdiff [81]. The expression profiles were clustered and visualized using in-house R scripts. Functional category analysis of differentially expressed genes was conducted using g:Profiler2 ver 0.2.0 [82] to gain insights into biological processes, KEGG pathways, and other functional gene sets. For gene set enrichment analysis (GSEA), transcriptomic data were normalized to $\log_2$-transformed TPM values and ranked by the signal-to-noise ratio between phenotypes. Lipidomic profiles were integrated by mapping identified lipid species to corresponding metabolic enzymes and pathways using molecular signature database (MSigDB), allowing linkage of lipid metabolic changes with transcriptomic alterations. The analysis was performed using GSEA version 4.3.2 (http://www.broadinstitute.org/gsea) with 1000 permutations, and phenotype labels defined as "high" and "low" expression groups for each hub gene. Predefined gene sets from MSigDB were interrogated, including KEGG_Arachidonic Acid_Metabolism, BIOCARTA _Eicosanoid _Pathway, PID_Lysophopholipids_Pathway. These were selected to capture the mechanistic link between PM-induced lipid remodeling and Mφ inflammatory activation. Significant enrichment was defined by FDR < 0.25 and nominal $p < 0.05$.

4.6. Lipidomic analysis

Untargeted lipid profiling was performed to analyze the lipid levels in Mφ and PM-Mφ cells using an Acquity ultraperformance liquid chromatography (UPLC, Waters) coupled with a Xevo G2-XS quadrupole

time-of-flight mass spectrometry (QTOF-MS, Waters) according to modified procedures previously used for adherent cells [83]. To extract intracellular lipids, 2×10^6 cells were quickly twice washed with PBS buffer and quenched in liquid nitrogen for 1 min. After the cells were scraped into 200 μL of cold methanol-water mixture (8:2, v/v), the extract was transferred into a 1.5 mL Eppendorf tube. This extraction step was repeated twice. The extract was vigorously mixed with 200 μL of water and 400 μL of chloroform for 1 min and then, kept at 4 °C for 30 min. After centrifuge at 21,191 ×g and 4 °C for 20 min, 350 μL of lower lipophilic solution was transferred into a new tube and dried under nitrogen gas. Powdered samples were stored at −80 °C until LC-MS analysis. Dried lipid metabolites were re-dissolved in 200 μL of isopropanol containing SPLASH LIPIDOMIX internal standard mix (Avanti Polar Lipids) and palmitic acid (U-13C16, 98 %, Cambridge Isotope Laboratories, Inc.). After dilution 5-fold for positive ion mode and 2-fold for negative ion mode with isopropanol-water mixture (8:2, v/v), 2 μL of each sample was injected into UPLC-QTOF-MS system. QC samples generated by pooling equal volume of each analytical sample were analyzed prior to running sample acquisition and between analytical samples. Intracellular lipids were separated using an Acquity UPLC CSH C18 column (100 mm × 2.1 mm, 1.7 μm particle size, Waters) at 55 °C and a flow rate of 0.4 mL/min. MS spectral data acquisition was performed in positive and negative electrospray ionization (ESI) modes with an *m/z* range of 50–1200. LC-MS data were processed using Progenesis software (Waters) to carry out peak finding, alignment, and generating peak tables of *m/z* and retention time. For further details, see Supplementary Information.

4.7. Quantitative reverse transcription PCR (qRT-PCR)

After total RNA was extracted with the RiboEX reagent, it was purified using a HybridR Kit (GeneAll) following the manufacturer's protocol. The RevertAid First-Strand cDNA Synthesis Kit (Thermo Fisher) was subsequently used to synthesize cDNA from 500 ng of purified total RNA. To conduct quantitative real-time PCR (qRT-PCR), we used the qTOWER3 Real-Time PCR Thermal Cycler (Analytik Jena) and TB Green Premix Ex Taq (Takara Bio). The cycle threshold (Ct) values were used to analyze the qPCR results, and we employed the $2^{-\Delta\Delta Ct}$ method for the analysis. The sequences of the primers used in this study are listed in Supplementary Table 2.

4.8. Quantitative assay for biological components

To evaluate TAG and cholesterol levels, the Colorimetric Serum Triglyceride Quantification Kit and the Colorimetric Total Cholesterol Assay Kit (Cell Biolabs) were used, respectively. To assess PGE2 and PGH2 levels in culture media, the PGE2 Parameter Assay Kit (R&D systems) and PGH2 CLIA Kit (Abbexa) were used, respectively. All the assays were performed following the manufacturer's instructions.

Statistical analysis

For statistical analysis, we utilized Microsoft Excel or GraphPad Prism ver. 8.0 software. To determine the significance of differences between two groups, we performed Student's t test using GraphPad Prism and Microsoft Excel. To evaluate the statistical significance of differences among multiple groups, we conducted one-way analysis of variance (ANOVA), followed by Tukey's multiple comparison test. The significance level was set at $p < 0.05$. For quantitative analysis of the relative FL intensity, the FL signal in cells was analyzed using ImageJ software by applying a segmentation algorithm to mask the cell boundary and stained areas (Otsu's method) and subsequently measuring the average integrated density within the cell boundaries. The quantified intensity values of the cells were then averaged.

Environmental implication

Exposure to PM triggers lipid-mediated inflammation in Mφ through the Lands cycle, a key phospholipid remodeling pathway. Our study demonstrates that PM exposure perturbs lipid homeostasis, leading to a pro-inflammatory state that may contribute to chronic inflammatory diseases. Given the widespread presence of airborne PM in urban environments, these findings underscore the urgent need for stricter air quality regulations to mitigate its impact on public health. Utilizing 3D-HT and multi-omics analysis, we provide a comprehensive real-time assessment of lipid metabolic alterations and inflammatory responses in living Mφ, offering novel insights into PM-induced pathophysiology.

CRediT authorship contribution statement

Jae-Hyuk Lee: Formal analysis, Data curation. **Yeongmi Cheon:** Formal analysis, Data curation. **Youngae Jung:** Formal analysis, Data curation. **Seul-Ki Mun:** Formal analysis, Data curation. **Seongsoo Lee:** Writing – review & editing, Writing – original draft, Visualization, Supervision, Resources, Investigation, Funding acquisition, Formal analysis, Conceptualization. **Hyun-Jin Kim:** Writing – review & editing, Writing – original draft, Visualization, Software, Methodology, Investigation, Data curation. **Su-Hyun Chae:** Formal analysis, Data curation. **JinO Shin:** Formal analysis, Data curation. **Jong-Jin Kim:** Formal analysis, Data curation. **Sung-Hak Kim:** Writing – review & editing, Writing – original draft, Visualization, Supervision, Resources, Investigation, Funding acquisition, Formal analysis, Conceptualization. **Jeongwon Park:** Writing – review & editing, Writing – original draft, Visualization, Software, Methodology, Investigation, Data curation. **Geum-Sook Hwang:** Writing – review & editing, Writing – original draft, Visualization, Supervision, Resources, Investigation, Funding acquisition, Formal analysis, Conceptualization. **Jueun Lee:** Writing – review & editing, Writing – original draft, Visualization, Software, Methodology, Investigation, Data curation.

Declaration of Competing Interest

The authors declare that they have no known competing financial interests or personal relationships that could have appeared to influence the work reported in this paper.

Acknowledgements

We are grateful to Dr. H Kim for providing the BV2 and Neuro2A cell lines and to Dr. SH Kim for providing the GL261 cell line. We also thank Dr. SM Lee, Dr. AR Kim and Dr. YH Kim for their technical assistance. This research was supported by the Basic Science Research Program of the National Research Foundation of Korea (NRF), funded by the Ministry of Education, Science, and Technology (2022R1I1A3070961 to SK) and the NRF grant funded by the Ministry of Science and ICT (NRF-2022R1A2C1005493 to SL, NRF-RS-2024–00345936 to GH). This research was supported by the Commercialization Promotion Agency for R&D Outcomes (COMPA) funded by the Ministry of Science and ICT (MSIT) (2710068936 to SL). This research was also supported by the Korea Basic Science Institute (No. C523100 to GH, C539143 to JL and C523310, C523400 to SL). This work was supported by the National Research Foundation (NRF) grant funded by the Korean government (MSIT) (RS-2025–02215830). The authors thank the Honam Regional Center of KBSI for experimental assistance with Low coherence holotomography system (HT-X1, OI26) and High Throughput Mitochondrial Function Analyzer (XFe96, KJ319). The authors also thank the Metropolitan Seoul Center of KBSI for allowing experimental assistance to the ultra-performance liquid chromatography- quadrupole time-of-flight mass spectrometry (UPLC-QTOF MS) (WS003 and WS005).

Appendix A. Supporting information

Supplementary data associated with this article can be found in the online version at doi:10.1016/j.jhazmat.2025.140027.

Data availability

The transcriptomic datasets generated in this study have been deposited in the NCBI Sequence Read Archive (SRA) under accession number PRJNA1173891. The lipidomics dataset generated in this study is publicly available in the Korea BioData Station (K-BDS) under the accession number KAP241530.

References

[1] Ning, J., et al., 2021. Association between ambient particulate matter exposure and metabolic syndrome risk: a systematic review and meta-analysis. Sci Total Environ 782, 146855.
[2] Sharma, P., et al., 2022. Particle uptake driven phagocytosis in macrophages and neutrophils enhances bacterial clearance. J Control Release 343, 131–141.
[3] Pramanik, S., Sil, A.K., 2023. Cigarette smoke extract induces foam cell formation by impairing machinery involved in lipid droplet degradation. Pflügers Arch Eur J Physiol 476, 59–74.
[4] Yan, M., et al., 2021. Exposure to particulate matter 2.5 and cigarette smoke induces the synthesis of lipid droplets by glycerol kinase 5. Clin Exp Pharm Physiol 48 (4), 498–507.
[5] Lee-Rueckert, M., et al., 2022. Lipid-Laden macrophages and inflammation in atherosclerosis and cancer: an integrative view. Front Cardiovasc Med 9, 777822.
[6] Safi, R., et al., 2023. Defensive-lipid droplets: cellular organelles designed for antimicrobial immunity. Immunol Rev 317 (1), 113–136.
[7] Kim, H., et al., 2024. Recent advances in label-free imaging and quantification techniques for the study of lipid droplets in cells. Curr Opin Cell Biol 87, 102342.
[8] Park, S., et al., 2020. Label-Free tomographic imaging of lipid droplets in foam cells for Machine-Learning-Assisted therapeutic evaluation of targeted nanodrugs. ACS Nano 14 (2), 1856–1865.
[9] Lee, W.S., et al., 2023. Three-dimensional label-free visualization of the interactions of PM2.5 with macrophages and epithelial cells using optical diffraction tomography. J Hazard Mater 456, 131678.
[10] Bosch, M., et al., 2020. Mammalian lipid droplets are innate immune hubs integrating cell metabolism and host defense. Science 370 (6514).
[11] Jarc, E., Petan, T., 2020. A twist of FATe: lipid droplets and inflammatory lipid mediators. Biochimie 169, 69–87.
[12] Yang, L., et al., 2021. PM(2.5) promoted lipid accumulation in macrophage via inhibiting JAK2/STAT3 signaling pathways and aggravating the inflammatory reaction. Ecotoxicol Environ Saf 226, 112872.
[13] Qin, S., et al., 2023. An integrative analysis of lipidomics and transcriptomics in various mouse brain regions in response to real-ambient PM(2.5) exposure. Sci Total Environ 895, 165112.
[14] Si, H., et al., 2023. Multi-omics reveals hypertrophy of adipose tissue and lipid metabolism disorder via mitochondria in young mice under real-ambient exposure to air pollution. Front Pharm 14, 1122615.
[15] Park, M., et al., 2024. The mechanism underlying correlation of particulate matter-induced ferroptosis with inflammasome activation and iron accumulation in macrophages. Cell Death Discov 10 (1), 144.
[16] Dijkhoff, I.M., et al., 2020. Impact of airborne particulate matter on skin: a systematic review from epidemiology to in vitro studies. Part Fibre Toxicol 17 (1), 35.
[17] Marek P., Elzbieta P.P., Andrea H., 2010.and , The Certification of the Mass Fractions of Selected Polycyclic Aromatic Hydrocarbons (PAHs) in Fine Dust (PM10-like Matrix) - Certified Reference Material ERM®-CZ100 ..
[18] Lim, C.Y., Zoncu, R., 2016. The lysosome as a command-and-control center for cellular metabolism. J Cell Biol 214 (6), 653–664.
[19] Correa Costa-Beber, L., et al., 2024. Aqueous PM(2.5) promotes lipid accumulation, classical macrophage polarisation and heat shock response. Chemosphere 363, 142987.
[20] Park, S.J., et al., 2019. Imaging inflammation using an activated macrophage probe with Slc18b1 as the activation-selective gating target. Nat Commun 10 (1), 1111.
[21] Muller, C., et al., 2018. Inhibition of cytosolic phospholipase A(2)alpha impairs an early step of coronavirus replication in cell culture. J Virol 92 (4).
[22] Zarrow, J.E., et al., 2022. Selective measurement of NAPE-PLD activity via a PLA (1/2)-resistant fluorogenic N-acyl-phosphatidylethanolamine analog. J Lipid Res 63 (1), 100156.
[23] Gaspar, A.H., Machner, M.P., 2014. VipD is a Rab5-activated phospholipase A1 that protects legionella pneumophila from endosomal fusion. Proc Natl Acad Sci USA 111 (12), 4560–4565.
[24] Norris, P.C., et al., 2014. Phospholipase A2 regulates eicosanoid class switching during inflammasome activation. Proc Natl Acad Sci 111 (35), 12746–12751.
[25] Raguenes-Nicol, C., et al., 1999. Anti-inflammatory mechanism of alminoprofen: action on the phospholipid metabolism pathway. Biochem Pharmacol 57 (4), 433–443.
[26] Aristizabal-Henao, J.J., et al., 2020. Lipidomics and environmental toxicology: recent trends. Curr Opin Environ Sci Health 15, 26–31.
[27] Shi, C., et al., 2024. Multi-omics integration analysis: tools and applications in environmental toxicology. Environ Pollut 360, 124675.
[28] Kim, S., Hollinger, H., Radke, E.G., 2022. Omics in environmental epidemiological studies of chemical exposures: a systematic evidence map. Environ Int 164, 107243.
[29] Cao, Y., et al., 2023. PPARgamma as a potential target for adipogenesis induced by fine particulate matter in 3T3-L1 preadipocytes. Environ Sci Technol 57 (20), 7684–7697.
[30] Shon, J.C., et al., 2020. Integrated metabolomics and lipidomics reveals high accumulation of polyunsaturated lysoglycerophospholipids in human lung fibroblasts exposed to fine particulate matter. Ecotoxicol Environ Saf 202, 110896.
[31] Yin, T., et al., 2022. Particulate matter Exposure-Induced cholesterol metabolism disorder in lung epithelial cells. Res Squrare.
[32] Zhao, C., et al., 2019. Omics approach reveals metabolic disorders associated with the cytotoxicity of airborne particulate matter in human lung carcinoma cells. Environ Pollut 246, 45–52.
[33] Wang, J., et al., 2023. Perturbation of arachidonic acid and glycerolipid metabolism promoted particulate matter-induced inflammatory responses in human bronchial epithelial cells. Ecotoxicol Environ Saf 256, 114839.
[34] O'Donnell, V.B., 2022. New appreciation for an old pathway: the lands cycle moves into new arenas in health and disease. Biochem Soc Trans 50 (1), 1–11.
[35] Guijas, C., et al., 2014. Phospholipase A2 regulation of lipid droplet formation. Biochim Biophys Acta 1841 (12), 1661–1671.
[36] Pol, A., Gross, S.P., Parton, R.G., 2014. Review: biogenesis of the multifunctional lipid droplet: lipids, proteins, and sites. J Cell Biol 204 (5), 635–646.
[37] Penno, A., Hackenbroich, G., Thiele, C., 2013. Phospholipids and lipid droplets. Biochim Biophys Acta 1831 (3), 589–594.
[38] Cabodevilla, A.G., et al., 2013. Cell survival during complete nutrient deprivation depends on lipid droplet-fueled beta-oxidation of fatty acids. J Biol Chem 288 (39), 27777–27788.
[39] Gubern, A., et al., 2009. Lipid droplet biogenesis induced by stress involves triacylglycerol synthesis that depends on group VIA phospholipase A2. J Biol Chem 284 (9), 5697–5708.
[40] Gubern, A., et al., 2008. Group IVA phospholipase A2 is necessary for the biogenesis of lipid droplets. J Biol Chem 283 (41), 27369–27382.
[41] Gubern, A., et al., 2009. JNK and ceramide kinase govern the biogenesis of lipid droplets through activation of group IVA phospholipase A2. J Biol Chem 284 (47), 32359–32369.
[42] Tan, S.T., et al., 2020. Emerging roles of lysophospholipids in health and disease. Prog Lipid Res 80, 101068.
[43] Murugesan, G., et al., 2003. Lysophosphatidylcholine regulates human microvascular endothelial cell expression of chemokines. J Mol Cell Cardiol 35 (11), 1375–1384.
[44] Olofsson, K.E., et al., 2008. Nanomolar concentrations of lysophosphatidylcholine recruit monocytes and induce pro-inflammatory cytokine production in macrophages. Biochem Biophys Res Commun 370 (2), 348–352.
[45] Ojala, P.J., et al., 2007. Acyl chain-dependent effect of lysophosphatidylcholine on human neutrophils. J Leukoc Biol 82 (6), 1501–1509.
[46] Endo Y., ,1-Oleoyl-lysophosphatidylethanolamine stimulates RORγt activity in TH17 cells. Science Immunology. 8(86): p. eadd4346.
[47] Law, S.-H., et al., 2019. An updated review of lysophosphatidylcholine metabolism in human diseases. Int J Mol Sci 20. https://doi.org/10.3390/ijms20051149.
[48] Schmitz, G., Ruebsaamen, K., 2010. Metabolism and atherogenic disease association of lysophosphatidylcholine. Atherosclerosis 208 (1), 10–18.
[49] Li, H., et al., 2025. Lysoglycerophospholipid metabolism alterations associated with ambient fine particulate matter exposure: insights into the pro-atherosclerotic effects. Environ Pollut 367, 125646.
[50] Olona, A., et al., 2021. Sphingolipid metabolism during Toll-like receptor 4 (TLR4)-mediated macrophage activation. Br J Pharm 178 (23), 4575–4587.
[51] Zierfuss, B., et al., 2022. Saturated very long-chain fatty acids regulate macrophage plasticity and invasiveness. J Neuroinflamm 19 (1), 305.
[52] Dabral, D., van den Bogaart, G., 2021. The roles of phospholipase A2 in phagocytes. Front Cell Dev Biol 9, **2021**.
[53] Elstad, M.R., et al., 1989. Platelet-activating factor acetylhydrolase increases during macrophage differentiation: a novel mechanism that regulates accumulation of Platelet-Activating factor. J Biol Chem 264 (15), 8467–8470.
[54] Rubio, J.M., et al., 2015. Group v secreted phospholipase A2 is upregulated by IL-4 in human macrophages and mediates phagocytosis via hydrolysis of ethanolamine phospholipids. J Immunol 194 (7), 3327–3339.
[55] Gil-de-Gómez, L., et al., 2020. Phospholipid arachidonic acid remodeling during phagocytosis in mouse peritoneal macrophages. Biomedicines 8. https://doi.org/10.3390/biomedicines8080274.
[56] Adolph, S., Fuhrmann, H., Schumann, J., 2012. Unsaturated fatty acids promote the phagocytosis of P. Aeruginosa and R. Equi by RAW264.7 macrophages. Curr Microbiol 65 (6), 649–655.
[57] Eijkelkamp, B.A., et al., 2018. Arachidonic acid stress impacts pneumococcal fatty acid homeostasis. Front Microbiol 9, **2018**.
[58] Roshanzadeh, A., et al., 2020. Surface Charge-Dependent cytotoxicity of plastic nanoparticles in alveolar cells under cyclic stretches. Nano Lett 20 (10), 7168–7176.
[59] Kim, G., et al., 2024. Holotomography. Nat Rev Methods Prim 4 (1).
[60] Chen, P., et al., 2023. Metabolic alterations upon SARS-CoV-2 infection and potential therapeutic targets against coronavirus infection. Signal Transduct Target Ther 8 (1), 237.
[61] Sumbria, D., et al., 2020. Virus infections and host Metabolism-Can we manage the interactions? Front Immunol 11, 594963.
[62] Haidar, Z., et al., 2023. Disease-associated metabolic pathways affected by heavy metals and metalloid. Toxicol Rep 10, 554–570.
[63] Yin, J., et al., 2022. Nanoplastics and microplastics May be damaging our livers. Toxics 10 (10).

[64] Maradonna, F., Carnevali, O., 2018. Lipid metabolism alteration by endocrine disruptors in animal models: an overview. Front Endocrinol (Lausanne) 9, 654.
[65] Medina-Ramirez, I.E., et al., 2024. Holotomography and atomic force microscopy: a powerful combination to enhance cancer, microbiology and nanotoxicology research. Discov Nano 19 (1), 64.
[66] Bresci, A., et al., 2024. Label-free morpho-molecular phenotyping of living cancer cells by combined Raman spectroscopy and phase tomography. Commun Biol 7 (1), 785.
[67] Jo, Y., et al., 2021. Label-free multiplexed microtomography of endogenous subcellular dynamics using generalizable deep learning. Nat Cell Biol 23 (12), 1329–1337.
[68] Jankowska-Kieltyka, M., et al., 2021. Metabolic response of RAW 264.7 macrophages to exposure to crude particulate matter and a reduced content of organic matter. Toxics 9. https://doi.org/10.3390/toxics9090205.
[69] Sun, Q., et al., 2005. Long-term air pollution exposure and acceleration of atherosclerosis and vascular inflammation in an animal model. JAMA 294 (23), 3003–3010.
[70] Park, J., et al., 2023. Artificial intelligence-enabled quantitative phase imaging methods for life sciences. Nat Methods 20 (11), 1645–1660.
[71] Vandereyken, K., et al., 2023. Methods and applications for single-cell and spatial multi-omics. Nat Rev Genet 24 (8), 494–515.
[72] Kim, S., et al., 2024. MiR-29 and MiR-140 regulate TRAIL-induced drug tolerance in lung cancer. Anim Cells Syst (Seoul) 28 (1), 184–197.
[73] Binkley, M.S., et al., 2020. KEAP1/NFE2L2 mutations predict lung cancer radiation resistance that can be targeted by glutaminase inhibition. Cancer Discov 10 (12), 1826–1841.
[74] Lee, S., et al., 2020. PTK2/FAK regulates UPS impairment via SQSTM1/p62 phosphorylation in TARDBP/TDP-43 proteinopathies. Autophagy 16 (8), 1396–1412.
[75] Yoo, C.J., et al., 2024. Complement receptor 4 mediates the clearance of extracellular tau fibrils by microglia. FEBS J 291 (15), 3499–3520.
[76] Otvos, B., et al., 2016. Cancer stem Cell-Secreted macrophage migration inhibitory factor stimulates myeloid derived suppressor cell function and facilitates glioblastoma immune evasion. Stem Cells 34 (8), 2026–2039.
[77] Shin, S., et al., 2015. Active illumination using a digital micromirror device for quantitative phase imaging. Opt Lett 40 (22), 5407–5410.
[78] Jiang, H., et al., 2014. Skewer: a fast and accurate adapter trimmer for next-generation sequencing paired-end reads. BMC Bioinforma 15 (182).
[79] Dobin, A., et al., 2013. STAR: ultrafast universal RNA-seq aligner. Bioinformatics 29 (1), 15–21.
[80] Trapnell, C., et al., 2010. Transcript assembly and quantification by RNA-Seq reveals unannotated transcripts and isoform switching during cell differentiation. Nat Biotechnol 28 (5), 511–515.
[81] Trapnell, C., et al., 2013. Differential analysis of gene regulation at transcript resolution with RNA-seq. Nat Biotechnol 31 (1), 46–53.
[82] Raudvere, U., et al., 2019. G:profiler: a web server for functional enrichment analysis and conversions of gene lists (2019 update). Nucleic Acids Res 47 (W1), W191–W198.
[83] Yeo, H.K., et al., 2021. Phospholipid transfer function of PTPIP51 at mitochondria-associated ER membranes. EMBO Rep 22 (6), e51323.